Journal of
Materials Chemistry C

ROYAL SOCIETY
OF CHEMISTRY

PAPER

View Article Online
View Journal | View Issue

Cite this: *J. Mater. Chem. C*, 2024, **12**, 2101

Rationalizing the carborane *versus* phenyl-driven luminescence in related dicarboxylic ligands and their antenna effect for their Eu^{3+} and Tb^{3+} metal–organic frameworks: a combined experimental and computational study†

Zhen Li,[ab] Claudio Roscini,[c] Rosario Núñez,[a] Francesc Teixidor,[a]
Clara Viñas,[a] Eliseo Ruiz*[d] and José Giner Planas*[a]

Replacement of a phenyl moiety by a carborane in 1,3-di(4-carboxyphenyl) derivatives has a pronounced effect on the photophysical properties of the compounds themselves and their corresponding Eu^{3+} and Tb^{3+} metal organic frameworks. Herein, we demonstrate that while the luminescence of the carborane-derivative 1,7-di(4-carboxyphenyl)-1,7-dicarba-closo-dodecaborane (*m*CB-L) is negligible in the solid state (0.3%), the corresponding phenyl-derivative [1,1′:3′,1″-terphenyl]-4,4″-dicarboxylic] (TDCA) is highly luminescent (quantum yield of 47.8%). However, the latter one is a much worse antenna for sensitizing Eu^{3+} and Tb^{3+} cations than the former one. Based on our previous studies where *m*CB-L behaves as a good antenna for these two lanthanides, we have now comparatively studied the optical properties of *m*CB-L and TDCA and their efficiency as sensitizers for Eu and Tb cations, in the solid state at room temperature. STEOM-DLPNO-CCSD calculations revealed a larger energy difference between the singlet S_1 and the lowest conical intersection (CI) points for TDCA (33.0 kcal mol^{-1}) than that for *m*CB-L (18.4 kcal mol^{-1}), explaining the observed different luminescence properties of these two compounds. Contrary to the carborane derivative, TDCA exhibits a more distorted structure at the CI point. TDCA-**Eu** and TDCA-**Tb** MOFs have been synthesized and characterized by infrared spectroscopy (IR) and powder X-ray diffraction (PXRD). The optical properties of TDCA-**Eu** and TDCA-**Tb** MOFs were investigated, and both MOFs displayed luminescence in the visible region with characteristic emission bands attributed to Eu^{3+} and Tb^{3+} transitions, respectively. However, the quantum yields for TDCA-**Ln** (Eu, 11.1%; Tb, 4.8%) were found to be much lower than those of carborane-based MOFs (Eu, 20.5%; Tb, 49.8%), indicating that the TDCA ligand is a less efficient light-absorbing sensitizer for Eu^{3+} and Tb^{3+} ions compared to the carborane-based ligand and may favor undesired back-energy transfer, as suggested by their faster decay times in comparison with the carborane counterparts. STEOM-DLPNO-CCSD calculations are used to analyze the changes in electron densities on photo-excitation from S_0 to S_1 and de-excitation from T_1 to S_0, as well as the differences in the excited state energies for *m*CB-L, TDCA, and the hypothetical longer derivatives (*m*CB-L2 and QDCA). Our research, which combines experimental and computational methods, offers valuable data for optimizing the singlet and triplet energies, as well as their differences (gaps), by choosing between phenyl and carborane as the building scaffold for 1,3-di(4-carboxyphenyl) compounds. This demonstrates that using phenyl or *m*-carborane as the building scaffold leads to distinct luminescence properties.

Received 3rd November 2023,
Accepted 4th January 2024

DOI: 10.1039/d3tc04018f

rsc.li/materials-c

---

[a] *Institut de Ciència de Materials de Barcelona (ICMAB-CSIC), Campus UAB, 08193 Bellaterra, Spain. E-mail: jginerplanas@icmab.es*

[b] *Shandong Provincial Key Laboratory of Monocrystalline Silicon Semiconductor Materials and Technology, College of Chemistry and Chemical Engineering, Dezhou University, Dezhou 253023, China*

[c] *Catalan Institute of Nanoscience and Nanotechnology (ICN2), CSIC, and The Barcelona Institute of Science and Technology (BIST), Campus UAB, Bellaterra, Barcelona 08193, Spain*

[d] *Departament de Química Inorgànica i Orgànica and Institut de Recerca de Química Teòrica i Computacional, Universitat de Barcelona, Diagonal 645, 08028 Barcelona, Spain. E-mail: eliseo.ruiz@qi.ub.es*

† Electronic supplementary information (ESI) available. See DOI: https://doi.org/10.1039/d3tc04018f

Introduction

Luminescent materials have attracted significant attention due to their wide-ranging applications in fields such as optoelectronics, photonics, and bioimaging.[1–5] The ability to control and manipulate the luminescent properties of materials is of utmost importance for designing advanced functional materials with tailored properties. In this context, the choice of molecular scaffolds as ligands plays a crucial role in determining the luminescent behavior of a material. To date, a predominant approach for designing organic fluorophores has been through conjugated systems, wherein diverse emitting units are interconnected by means of double bonds, triple bonds, and aromatic rings.[6]

In recent years, icosahedral *closo*-carboranes 1,*n*-$C_2B_{10}H_{12}$ (n = 2, 7 or 12), which are molecular carbon–boron polyhedral clusters, have emerged as promising building blocks for a wide variety of applications.[7–13] Carboranes, as boron-rich clusters with three-dimensional aromatic structures,[14–16] exhibit exceptional stability and possess advantageous material properties such as robust thermal and chemical stability, as well as notable hydrophobicity.[7,10,11,17–21] We and others have demonstrated that carboranes are excellent scaffolds in luminescent materials both in solution[9,22–32] and, more recently, in the solid state.[33–38] Regarding the latter, in recent years significant progress has been made in the development of carborane-based active luminophores,[39] which exhibit properties that align with solid-state luminescence and stimuli-responsiveness. This indicates that the luminescent features, including the color, can be adjusted by manipulating the molecular morphology in the solid and aggregate states. By utilizing these adjustable luminescent properties, it is possible to create unique stimuli-responsive luminescent materials using carborane based molecules. Our group has recently contributed to this area of research through the development of highly emissive water dispersible nanoparticles,[40] fluorescent metal complexes with unique structures[41] and luminescent lanthanide metal–organic frameworks (Ln-MOFs) that are printable from water inks for potential applications in anticounterfeiting and bar-coding.[42] However, the vast majority of luminescent materials in aggregate or solid state based on carboranes are associated with the *ortho*–*closo*-carborane (1,2-$C_2B_{10}H_{12}$) isomer or its *nido*-carborane derivatives ($C_2B_9H_{12}^-$),[36,43] while only a limited number of examples have been reported for the *m*eta-carborane (1,7-$C_2B_{10}H_{12}$; Chart 1) isomer, mostly from our group.[41,42,44–48] Carboranes are often viewed as three-dimensional analogues to benzene (Chart 1, top).[41,48] The former are significantly larger (∼40%) than the benzene ring rotation envelope[10] and behave as strong electron-withdrawing groups (similar to a fluorinated aryl) on a substituent at one of the cluster carbons.[10,49–51] The replacement of a phenyl moiety by a carborane in a molecule can have a significant impact on the vertical excitation processes, including the electronic structure, optical properties, and excited-state behavior of the molecule. Given the distinctive features of carboranes and phenyl rings as molecular scaffolds, a comparative study of their luminescence and vertical excitation properties would provide valuable insights into their potential as ligands for designing luminescent materials.

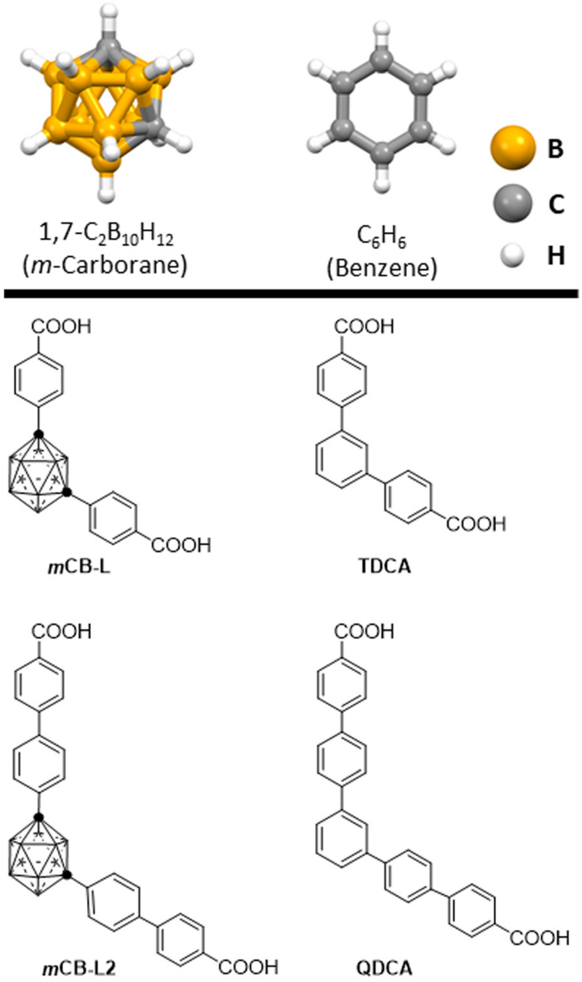

Chart 1 A representation of *m*-carborane and benzene (top) and dicarboxylic acids studied in this work (bottom).

Here, we present a comparative study of luminescence and vertical excitation properties of carborane-based and phenyl-based ligands themselves, and their corresponding Eu^{3+} and Tb^{3+} metal organic frameworks. In this study, two 1,3-di(4-carboxyphenyl) derivatives were experimentally examined (1,7-di(4-carboxyphenyl)-1,7-dicarba-*closo*-dodecaborane (*m*CB-L) and [1,1′:3′,1″-terphenyl]-4,4″-dicarboxylic (TDCA); Chart 1). These two compounds differ in their central moiety, with one having a 2D aromatic phenyl ring (TDCA), and the other having a 3D aromatic carboranyl moiety (*m*CB-L). These materials exhibit differences in their photoluminescence quantum yields and their ability to act as antennas for Eu^{3+} and Tb^{3+} cations in the solid state. To prove this, we have synthesized and characterized the corresponding TDCA-**Eu** and TDCA-**Tb** MOFs. We have combined experimental approaches and a recently developed similarity transformed equation-of-motion domain-based local pair natural orbital coupled-cluster singles and doubles (STEOM-DLPNO-CCSD) theoretical method (see Computational details section), and determined that the molecular structures play a crucial role in the corresponding energy levels of the excited states and therefore in the photophysical properties of these carboxyphenyl and carboxycarboranyl derivatives and their corresponding lanthanide metal organic frameworks. extended *m*CB-L2 and QDCA compounds have also been studied by computational methods.

Results and discussion

We have investigated the optical properties of TDCA by UV-vis absorption and emission spectroscopies in the solid-state at room temperature. The free TDCA compound exhibits a broad absorption band centered around 300 nm (Fig. S1, ESI†), which is attributed to the $\pi \rightarrow \pi^*$ transitions. The luminescence spectrum for TDCA upon continuous-wave irradiation (λ_{ex} = 290 nm) shows a strong emission at λ_{em} = 390 nm and an overall quantum yield (Φ) of 47.8% (Fig. S2, ESI†). As summarized in Table 1, the observed Φ for TDCA is much larger than that for the carborane derivative *m*CB-L (0.3%).[42] In order to understand the photophysical properties of these two related derivatives, we have calculated their ground state electronic structures and vertical excitation energies. We have performed the calculations by using the recently developed coupled cluster method STEOM-DLPNO-CCSD. This is a wave function-based quantum chemistry approach based on coupled cluster calculation,[52] which gives accurate results for the prediction of excited energy values.[53] The calculated values of singlet (S) and triplet (T) levels for *m*CB-L and TDCA are summarized in Table 1. Similar results regarding the energy differences S_0–S_1 and T_1–S_0 for TDCA and *m*CB-L1 ligands were obtained at both B3LYP-TDDFT[42] and STEOM-DLPNO-CCSD level of theory (Table S1, ESI†). We have computed the vertical and adiabatic excitation energies.[54] For *m*CB-L, the vertical S_1 excitation energy of 272 nm is in agreement with the experimental value determined for this compound in the solid state with a $\lambda_{max}^{abs} \sim$ 289 nm. The lowest energy of the S_1 vertical excitation than the adiabatic value is due to differences between the potential surfaces between DFT and the coupled cluster method. For TDCA, the S_1 excitation energy values are 280 and 294 nm (vertical and adiabatic values, respectively, see Table S2, ESI†), also very close to the experimental broad absorption band centered around 300 nm.

To better comprehend the contrasting luminescent behavior in the solid state exhibited by TDCA and *m*CB-L, we conducted a comprehensive investigation into the deexcitation process *via* conical intersections (CI), which denotes points where the potential energy surfaces of two electronic states intersect (Fig. 1).[55–58] The kinetics of non-radiative decay crucially relies on the presence of CI. Hence, the accessibility of CI directly impacts the rates of non-radiative decay and, consequently, the fluorescence quantum yield. Fig. 1 portrays schematic representations of two distinct potential energy profiles: one indicating the dominance of non-radiative decay (Fig. 1a), and the other highlighting the predominance of radiative decay with fluorescence (Fig. 1b). In Fig. 1a, a minimum energy CI is observed in a lower energy region relative to the Franck–Condon (FC) point, thereby facilitating rapid, non-radiative decay through the corresponding CI region. Conversely, in Fig. 1b, the lowest energy CI is situated significantly higher in energy compared to the FC point, resulting in infrequent access of the molecule to the CI region and consequently slower non-radiative decay. By comparing the energy differences between the singlet S_1 states and the optimized CI structures of the investigated molecules, one can elucidate the relative significance of radiative *versus* non-radiative decay. We have therefore explored the minimum energy CI structures of TDCA and *m*CB-L. The geometries corresponding to the conical intersections were also optimized at the TDDFT-B3LYP level (Fig. 1c, d and Experimental section). The energy differences between the singlet S_1 and the optimized conical intersection structures were then calculated at DLPNO-CCSD level. A much larger difference was found for TDCA (33.0 kcal mol^{-1}) than for *m*CB-L (18.4 kcal mol^{-1}). Consequently, the energy barrier between the singlet S_1 and the lowest CI point decreases when replacing a phenyl ring by a carborane moiety as the central core of 1,3-di(4-carboxyphenyl) derivatives. Analysis of the structures at the conical intersection points reveals notable differences in geometries between the two systems, as shown in Fig. 1c and d. The TDCA ligand exhibits a quite distorted structure that deviates from planarity, whereas the *m*CB-L compound does not show any distortion. These findings confirm that the *m*-carborane-based system, with a smaller energy difference at the CI point, may facilitate a more accessible non-radiative process compared to the phenyl-based system.

Table 1 Comparison of solid-state fluorescence parameters, ground and excited electronic energies for TDCA and *m*CB-L compounds at STEOM-DLPNO-CCSD level of theory using DFT optimized structures. The results are vertical (in italic) and adiabatic (in bold) excitations

	Experimental			Calculated	
Compounds	λ_{ex} (nm)	λ_{em} (nm)	Φ (%)	S_0–S_1 nm (cm^{-1})	T_1–S_0 nm (cm^{-1})
TDCA	290	390	47.8	*280 (35 727)* **294 (34 065)**	*624 (16 033)* **476 (20 989)**
*m*CB-L	280	312	0.3	*272 (36 806)* **241 (41 437)**	*526 (19 006)* **424 (23 593)**

We also wondered how the replacement of carborane by a phenyl moiety might affect the vertical excitation processes in these 1,3-di(4-carboxyphenyl) derivatives. Fig. 2 shows a representation of the change of electron densities on photoexcitation from S_0 to S_1 and Fig. S3 (ESI†) represents the de-excitation from T_1 to S_0 obtained from the STEOM-DLPNO-CCSD calculations. Lobes in Fig. 2 and Fig. S3 should not be confused with the common HOMO–LUMO orbitals. Lobes in these figures represent electron density differences between the initial and the final state, and the color relates to loss (purple) or a gain (pale brown) of electron density through the excitation or de-excitation processes. Thus, during the vertical S0 → S1 photo-excitation of *m*CB-L, there is a net electron density transfer from the phenyl rings toward the carboxylic acids (Fig. 2). The absence of a lobe in the carborane moiety means that its electron density change on excitation is zero, although the carborane orbitals do participate.[42] In the case of the TDCA, there is an involvement of the three aromatic rings, indicating

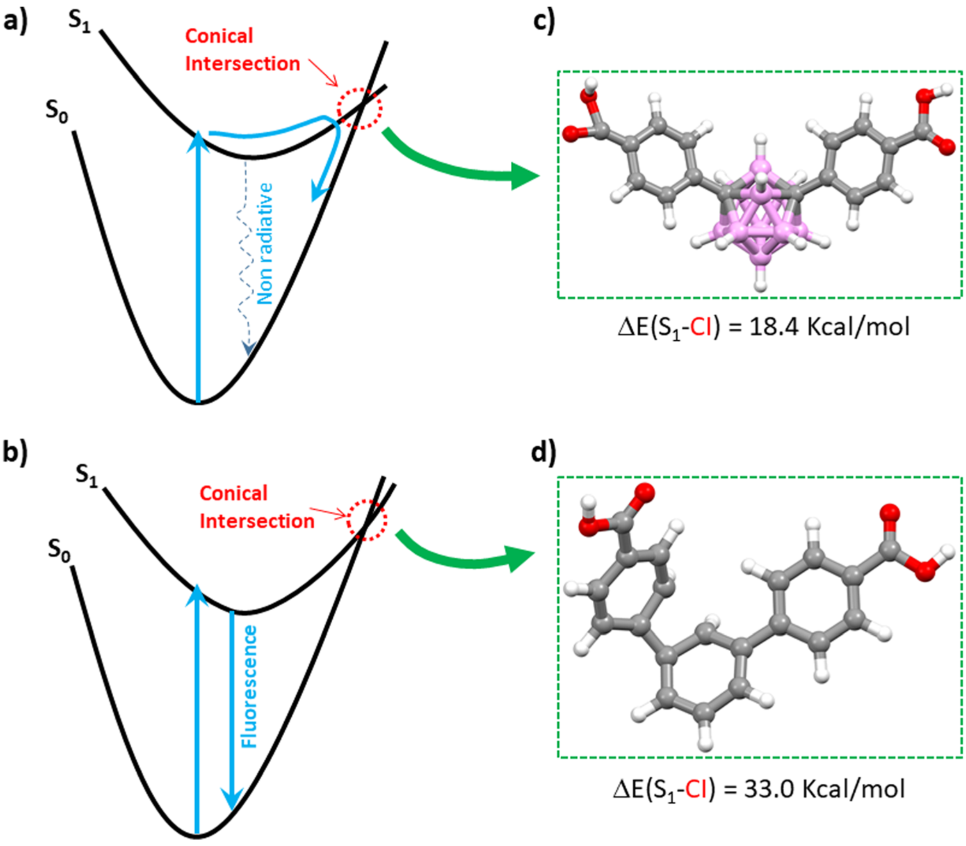

Fig. 1 Schematic representation of the potential energy surfaces for two types of photo-excitations and geometries of the studied molecules optimized at the conical intersection points. (a) The case in which an ultrafast non-radiate decay *via* the conical intersection (CI) region (see dotted blue arrow) is dominant. (b) The case in which the decay *via* a fluorescence process (solid blue arrow) is dominant. Views of *m*CB-L (c) and TDCA (d) optimized molecular structures at their CI points. Fig. 1a and b is adapted from ref. 46 with permission from the Royal Society of Chemistry. Color codes for atoms in the structures: C, gray; H, white; O, red; B, pink.

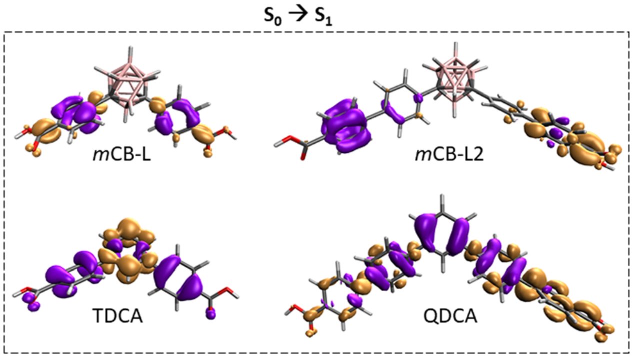

Fig. 2 Schematic diagrams for the energy absorption on photoexcitation from singlet states (S_0 to S_1). Purple (negative values) and pale brown (positive values) lobes represent the electron density differences between the initial and final state calculated at STEOM-DLPNO-CCSD level.

that on excitation, the transfer occurs from the external aromatic rings to the central one, being the electron density concentrated in the central phenyl group. The different electron density transfer between these two closely related molecules is probably due to their different symmetry, being *m*CB-L the less symmetrical. The analysis of the net electron density transfer on vertical $S_0 \rightarrow S_1$ excitation of the longer molecules (*m*CB-L2 and QDCA; Chart 1) revealed clear differences between them and with their shorter counterparts. *m*CB-L2 shows a net electron density transfer from the two consecutive phenyl rings from one side of the molecule toward the rings in the other side. As in *m*CB-L, the carborane moiety shows an imperceptible electron density change. The QDCA shows an electron density transfer between the three central phenyl rings towards the phenylcarboxylic moieties at the extremes of the molecule.

Although *m*CB-L shows negligible fluorescence in the solid state, it was shown to behave as a good antenna ligand for Eu^{3+} and Tb^{3+}.[42] Such lanthanide cations are highly adaptable for use in lighting and sensing applications, but their effectiveness depends on the presence of an efficient antenna due to their low absorption capability.[59,60] We previously reported a strong luminescence of *m*CB-**Eu** and *m*CB-**Tb** MOFs,[42] which indicates that in the presence of any of these two lanthanide cations, excitation of *m*CB-L is followed by intersystem crossing (ICS) from its singlet state (S_1) to the triplet excited state (T_1) and subsequent energy transfer (ET) from T_1 of *m*CB-L to the emissive levels of the metals, thus originating the observed metal-centered emissions.[42] Even though this is the more accepted intramolecular ET process (also known as *antenna effect*) for lanthanide complexes and MOFs, a number of reports have shown that the ET can also be originated from the singlet state S_1 (or charge transfer (CT) state) to the emissive levels of the metals.[61–63] Nevertheless, the lowest STEOM-DLPNO-CCSD calculated excited states energies for TDCA and *m*CB-L (Table S2, ESI†) show, in agreement with our previous prediction based on time-dependent density functional theory (TDDFT) methods (Table S1, ESI†), that the energies of the S_1 and T_1 states for TDCA are lower than those for *m*CB-L. The latter indicates that energy transfer is expected to be much less efficient in the case of the TDCA ligand, as the energy of its triplet state is slightly lower than that of Eu^{3+} and much lower than that of Tb^{3+} (*vide infra*). In order to verify this prediction, we have synthesized a series of lanthanide MOFs based on the TDCA ligand and studied their photophysical properties.

Needle-like $\{[Ln_2(TDCA)_3(DMF)]_n{\cdot}Solv\}$ (TDCA-**Ln**, where Ln = Eu, Tb) crystals were prepared by a solvothermal reaction between the TDCA ligand and the corresponding lanthanide nitrate in a mixture of DMF/HNO_3 at 175 °C for 3 days (Fig. S5, ESI†). Infrared spectra (IR) and powder X-ray diffraction (PXRD) for TDCA-**Eu** and TDCA-**Tb** match well with the reported for TDCA-**Ce**[64] and proved to be isostructural (Fig. S5 and S6, ESI†, respectively). Although the 3D structures of the latter differ to those for the carborane based MOF family, they all consist of 1D rod-shaped LnOx polyhedral, with carboxylate linkers coordinating in a bridging mode.[64] The optical properties of TDCA-**Ln** (Ln = Eu, Tb) were investigated by measuring their UV-vis absorption (Fig. S1, ESI†) and emission spectra (Fig. 3 and Table 2) in the solid state at room temperature. Both MOFs display similar broad absorption bands to that of the free ligand, with the peak maximum slightly blue shifted to 290 nm (Fig. S1, ESI†). The luminescence spectra for TDCA-**Eu** (λ_{ex} = 290 nm) displays red luminescence with well-resolved emission bands in the visible region at 591, 614, 650 and 699 nm (Fig. 1a), attributed to the characteristic Eu^{3+} transitions ($^5D_0 \rightarrow {}^7F_J$; J = 1–4). These emission bands were similar to those of carborane-based analogue ***m*CB-Eu**.[42] No emission bands were observed in the UV region, indicating a good quenching of the luminescence of the ligand. Contrary to the TDCA-**Eu** MOF, the related TDCA-**Tb** compound exhibits the simultaneous luminescence of the TDCA ligand and the Tb^{3+} ions upon excitation at 290 nm (Fig. 3b). The emission spectrum of TDCA-**Tb** shows a weak blue emission band centered at 377 nm, ascribed to the $\pi \rightarrow \pi^*$ transitions of the ligand, and sharp bands at 489, 541, 582, and 621 nm, typical of the Tb^{3+} transitions ($^5D_4 \rightarrow {}^7F_J$ (J = 6–3). The lifetimes (τ) and Φ for TDCA-**Eu**, TDCA-**Tb** are summarized in Table 2. As can be seen in Table 2, Φ for TDCA-**Eu** and TDCA-**Tb** are 11.1% and 4.8%, respectively. Slight variations of the excitation wavelength (280–310 nm) show rather consistent Φ values and emission spectra (Fig. S7, ESI†). Mono-exponential fitting of the slower part of the decay curves was carried out to obtain the longest luminescence lifetimes, while avoiding possible background interferences. The obtained lifetimes for the TDCA MOFs resulted quite shorter than those of the corresponding *m*CB-**Ln** MOFs, as shown in the Table 2.

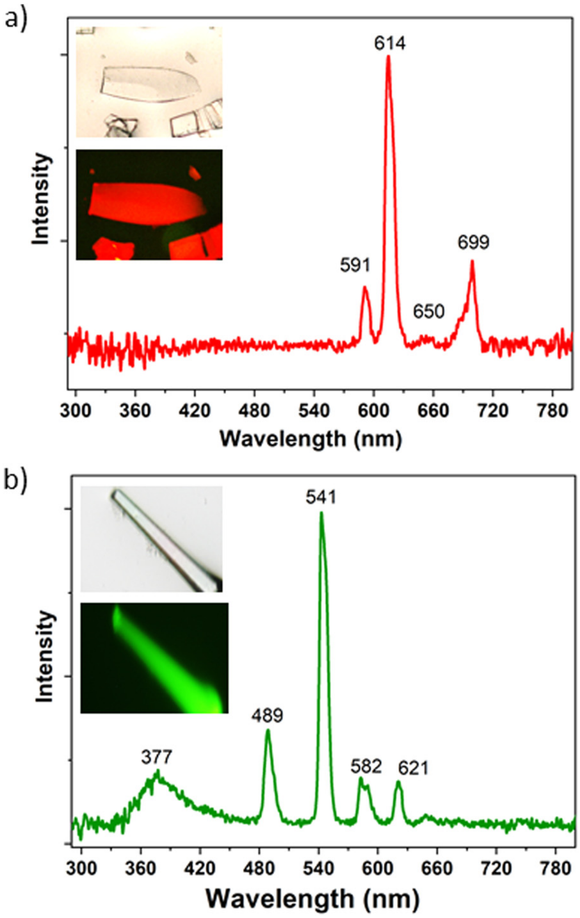

Fig. 3 Solid-state emission spectra of TDCA-**Eu** (a) and TDCA-**Tb** (b) under continuous-wave irradiation (λ_{ex} = 290 nm) at room temperature. Insets: Optical microscopy images of the corresponding crystals under white and the corresponding luminescence images).

Table 2 Comparison of solid state fluorescence parameters for TDCA-**Eu**, TDCA-**Tb**, *m*CB-**Eu** and *m*CB-**Tb**

MOF	λ_{em} (nm)	Φ (%)	τ (μs)
TDCA-**Eu**[a]	591, 614, 650, 699	11.1	387.7
*m*CB-**Eu**[b]	591, 614, 650, 699	20.5	739.0
TDCA-**Tb**[a]	377, 489, 541, 582, 621	4.8	61.5
*m*CB-**Tb**[b]	489, 541, 582, 621	49.8	849.7

[a] This work; λ_{ex} = 290 nm. [b] Ref. 42 λ_{ex} = 280 nm.

The shorter lifetimes of the TDCA-**Ln** MOFs suggest the presence of quenching effects of the sensitized Ln luminescence (Fig. S8, ESI†). Since both types of MOFs (TDCA-**Ln** MOFs and *m*CB-**Ln** MOFs) are measured in the same conditions and in the solid state, external causes for quenching (*e.g.* solvent) should be excluded. Thus, a plausible explanation could be related to the back-energy transfer from the Ln to the ligand, mainly occurring in the TDCA-based MOFs. This is also supported by the lower quantum yield values of these MOFs, compared to the *m*CB-based MOFs. If part of the energy of the Ln is quenched by the back-energy transfer, the amount of energy released through radiative decay is reduced, decreasing the value of the luminescence quantum yield. Nevertheless, the lower Φ values for the phenyl based TDCA-**Ln** than the related carborane based *m*CB-**Ln** MOFs could be also ascribed to less efficient direct energy transfer from the TDCA ligand to the Ln (for sensitizing both Ln^{3+} cations), compared to the *m*CB-L ligand. The observed broad blue emission for TDCA-**Tb** indicates that for this particular ion, the energy absorbed by the TDCA ligand is not completely transferred to the Tb^{3+} cations in the solid state. The absence of such blue emission for TDCA ligand in TDCA-**Eu** indicates a better energy transfer to the metal ion.

The above experimental data clearly corroborates our computational predictions. That is, the TDCA ligand is much worse antennae than the carborane based ligand *m*CB-L. Fig. 4 summarizes the STEOM-DLPNO-CCSD calculated S_1, T_1 energy values and gaps (ΔE_{S-T}) for *m*CB-L, TDCA and two hypothetical ligands *m*CB-L2 and *m*QDCA which are the result of adding two additional aromatic rings to the previous ones (Chart 1). Efficient lanthanide-centered luminescence of MOFs is fulfilled by the use of antenna linkers with the lowest triplet state of the organic linkers located at least 1850 cm^{-1} above the lowest emitting excited states of the lanthanide ions.[65] Regarding the family of isostructural lanthanide (Eu^{3+} and Tb^{3+}) MOFs containing *m*CB-L, the T_1 energy level of the carborane ligand was calculated to be 23 593 cm^{-1} and thus capable of sensitizing both cations (Eu^{3+}, 17 300 cm^{-1}; Tb^{3+}, 20 500 cm^{-1}; Fig. 4). In the case of the TDCA ligand, its T_1 energy level is calculated to be 20 989 cm^{-1}, that is, 489 cm^{-1} above that for the Tb^{3+} excited state and 3689 cm^{-1} above that for Eu^{3+}. The very much lower T_1 energy of TDCA than that for *m*CB-L explains the more ineffective ET and the experimental observation of the free ligand emission and very weak Tb-centered emission (Fig. 3 and Table 2). In other words, the higher energy of T_1 for *m*CB-L than that for TDCA allows to sensitize the emissive state of the Tb^{3+} cations, explaining the 10 times-fold quantum yield for the former one. The quantum yield difference between *m*CB-**Eu** and TDCA-**Eu** is less pronounced as the corresponding ligands T_1 energies are well above the resonance level of the Eu ions in these cases. In the case of Ln-MOF formation of the two hypothetical ligands (*m*CB-L2 or QDCA, Chart 1), their very much lower T_1 energies (Table S2, ESI† and Fig. 4) suggest that the QDCA ligand would be able to sensitize only Eu^{3+}, while the *m*CB-L2 would not be acting as a good antenna for any of these two cations.

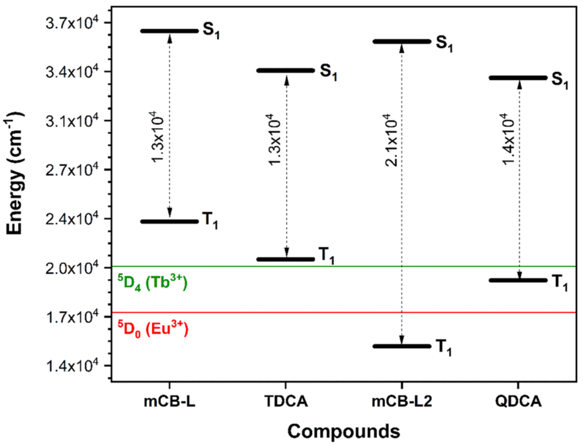

Fig. 4 Dependence of the STEOM-DLPNO-CCSD calculated S_1, T_1 and energy gap (dashed grey arrows) values as a function of the molecular structures. Energies of the lowest emitting excited states of Tb^{3+} and Eu^{3+} are indicated as green and red lines, respectively.

With regards to the STEOM-DLPNO-CCSD calculated minimum excited state energies for the extended compounds *m*CB-L2 and QDCA (Fig. 4 and Tables S1–S2, ESI†), the results indicate that the replacement of a central phenyl moiety by a 3-D *m*-carborane cluster increases the S_1 energies (Fig. 4). Those energies are however rather uniform within the same series of ligands (*m*CB-L, 36 806 cm^{-1}/*m*CB-L2, 36 080 cm^{-1} *versus* TDCA, 34 065 cm^{-1}/QDCA, 33 565 cm^{-1}). We found however a higher variability in the calculated minimum T_1 excited energies, as can be seen in Fig. 4. There is a decrease of the T_1 energies of the compounds in the order *m*CB-L > TDCA > QDCA > *m*CB-L2. Thus, one could "modulate" the energy gaps (ΔE_{S1-T1}) by selecting the appropriate molecular structure of the ligand. Controlling the energy gaps between the S and T states is essential in the development of energy-efficient light-emitting diodes, various solar energy conversion methods, and photocatalytic transformations.[66–68] Our data reveals that the shorter *m*CB-L and TDCA ligands show the smallest energy gaps (13 213 and 13 076 cm^{-1}, respectively; Table S2, ESI† and Fig. 4), than the longer ligands QDCA (14 034 cm^{-1}) and *m*CB-L2 (21 148 cm^{-1}). The smaller gap of *m*CB-L, in addition to the high energy of its T1 state, explains the much better efficiency of this ligand as good antennae for the studied cations. It has been demonstrated that the intersystem crossing (ISC) efficiency can be improved by reducing the energy gap between S_1 and T_1 (ΔE_{S1-T1}).[69,70] However, we cannot exclude a simultaneous ET process from S_1 to the emitting states of the lanthanide ions.[62] In such scenario (simultaneous S_1 and T_1 ET to Lanthanide cations), the observed changes in electron densities on vertical singlet excitations between *m*CB-L and TDCA (Fig. 2 left) are worth commenting as those may have an impact on the observed lanthanide based luminescence. On excitation, the electron density transfer takes places from the phenyl rings in *m*CB-L to the carboxylic acids, so that such electron density could be further transfer to the lanthanide cations on coordination. Such electron density transfer would not happen, or at least not preferentially, in the case of TDCA. All these might also explain why the carborane based linker is a much better antenna for Eu^{3+} and Tb^{3+} than the corresponding phenyl based linker.

We highlight the use of STEOM-DLPNO-CCSD calculations in conjunction with experimental findings to showcase how the replacement of a planar phenyl group with a 3D carborane fragment produces a significant impact in the photophysical properties of both the ligands and their lanthanide metal–organic frameworks (MOFs).

Conclusions

In conclusion, the TDCA ligand exhibited strong fluorescence with a high quantum yield in the solid state at room temperature, which is basically quenched when replacing the central phenyl moiety in TDCA by a carborane moiety (*m*CB-L). Quantum chemistry calculations (STEOM-DLPNO-CCSD and B3LYP-TDDFT) provided insights into the electronic structures and excited state energies of TDCA and *m*CB-L, indicating that the *m*-carborane-based *m*CB-L ligand may have a more accessible non-radiative decay process compared to the phenyl-based TDCA ligand. It was found that structural deformation in the minimal energy conical intersection (CI) was localized on a single phenyl ring of the TDCA, that was not taking place in the corresponding carborane derivative *m*CB-L. The findings highlight the importance of the molecular structure and symmetry in determining the photophysical properties of 1,3-di(4-carboxyphenyl) derivatives in the solid state.

TDCA-**Ln** (Ln = Eu, Tb) MOFs were successfully synthesized and their optical properties were investigated. TDCA-**Eu** displayed red emission with sharp and well-resolved emission bands at 591, 614, 650, and 699 nm, characteristic of Eu^{3+} transitions, while TDCA-**Tb** exhibited simultaneous luminescence of the TDCA ligand and Tb^{3+} ions with emission bands at 489, 541, 582, and 621 nm, typical of Tb^{3+} transitions. However, the quantum yields for TDCA-**Eu** and TDCA-**Tb** were found to be much lower than those of carborane-based MOFs, indicating that the TDCA ligand is a less efficient light-absorbing antenna chromophore for sensitizing Eu^{3+} and Tb^{3+} ions compared to the carborane-based ligand. However, the faster and multiexponential decays of the TDCA MOFs indicate the presence of back energy-transfer, which could also contribute to the lower quantum yield values. The observed broad blue emission at 377 nm for TDCA-**Tb** suggests that the energy absorbed by the TDCA ligand is not completely transferred to the Tb^{3+} ions in the solid state. Computational calculations also supported the experimental results, showing that the TDCA ligand has a lower triplet energy level compared to the carborane-based ligand, which could result in the lower quantum yields observed for TDCA-**Ln** compounds.

This study provides insights into how the replacement of carborane by a phenyl moiety affects the vertical excitation processes in 1,3-di(4-carboxyphenyl) derivatives. The analysis of electron density changes on photo-excitation and de-excitation using STEOM-DLPNO-CCSD calculations reveals differences in electron density transfer between the carborane-based and phenyl-based derivatives. The findings suggest that the electron density transfer from the phenyl rings to the carboxylic acids upon excitation may play a role in the observed luminescence properties of lanthanide-based metal–organic frameworks (MOFs) containing carborane-based linkers. The use of wave function-based quantum chemistry calculations in conjunction with experimental results provides valuable insights into the photophysical properties of these compounds and their potential applications in luminescent materials.

Experimental section

All chemicals were of reagent-grade quality. They were purchased from commercial sources and used as received.

Synthesis of $\{[(Ln)_2(TDCA)_3(DMF)_x]_n{\cdot}Solv\}$ (TDCA-Ln, where TDCA = [1,1′:3′,1″-terphenyl]-4,4″-dicarboxylic])

A solvothermal method was adopted to prepare the TDCA-Ln crystal. Briefly, 0.02 mmol of $Ln(NO_3)_3$ (Ln = Ce, Eu or Tb) and 0.03 mmol of TDCA ligand were dissolved in 0.5 mL of DMF with the help of sonication. 7 μL of concentrated HNO_3 was added into the above mixture. The above solution was further transferred to an 8-dram vial and heated at 175 °C in an oven for 72 h. The colorless crystals were obtained after washing with DMF and methanol for several times (Yield based on the Ln^{3+} cation: 42.7% for TDCA-**Ce**, 36.2% for TDCA-**Eu** and 33.7% for TDCA-**Tb**). Elemental analysis (%): calculated for $\{Ce_2(TPDC)_3(DMF)_5]_n{\cdot}18H_2O\}$: C 46.91, H 5.58, N 3.65; found: C 47.00, H, 4.16, N 3.64; calculated for $\{Eu_2(TPDC)_3(DMF)_4]_n{\cdot}5H_2O{\cdot}4MeOH\}$: C 51.55, H 5.09, N 3.16; found: C 51.41, H, 3.94, N 3.05; calculated for $\{Tb_2(TPDC)_3(DMF)_3]_n{\cdot}8H_2O{\cdot}2MeOH\}$: C 50.53, H 4.80, N 2.49; found: C 50.20, H, 3.82, N 2.45.

Instruments and characterization. Emission spectra and quantum yields (Φ) of solid-state samples under steady excitation (λ_{ex} = 290–310 nm) were determined using a quantum yield fluorimeter (Hamamatsu C9920-02G, equipped with an integrating sphere) at room temperature in the air. Fluorescence decay curves were recorded on a PTI Quantamaster 300 fluorimeter at an excitation of 290 nm with a pulsed Xe lamp (100 Hz, 2 μs integration time). The mono-exponential model function was adopted to fit the decay curves (Fig. S8, ESI†). Attenuated total reflection Fourier transform infrared (ATR-FTIR) spectra were obtained by using a PerkinElmer Spectrum One spectrometer. Elemental analyses were carried out in a Thermo (Carlo Erba) Flash 2000 Elemental Analyzer, configured for wt % CHN. Powder X-ray diffraction (PXRD) was recorded at room temperature on a Siemens D-5000 diffractometer with Cu Kα radiation (λ = 1.5418 Å).

Computational details. To improve the understanding of the photochemistry of the studied ligands computational methods have been employed. Previously, we studied the properties of some of these systems by using TDDFT calculations.[42] In order to improve the methodology in the present study, a coupled-cluster method was employed by using Orca 5.0.2 code[71] using the similarity transformed equation of motion approach combined with the domain-based local pair orbital implementation of coupled-cluster singles and doubles method, STEOM-DLPNO-CCSD,[72–78] to calculate the state energies. The general def2-TZVP basis set was employed together with auxiliary basis sets def2-TZVP/C and def2/J for the MP2 and Coulomb integrals, respectively.[74,79] The geometries were optimized by the Gaussian 16 program[80] with the exchange–correlation functional B3LYP[81] and a 6-311G* basis set using the TDDFT option for the excited state optimization. Such exchange–correlation functional provides a better description of the excitation energies for some of the studied systems at TDDFT level than other hybrid ones. Conical intersection geometries were calculated with the same TDDFT approach but using Orca 5.0.2 code.[71] Neutral molecules including the acidic hydrogen atoms were employed to have a closer description of the electronic structure of the metal-coordinated ligands than simply the anionic ligands.

Conflicts of interest

There are no conflicts to declare.

Acknowledgements

This work was financially supported by MICINN (PID2019-106832RB-I00, PID2021-122464NB-100, PID2022-136892NB-I00), and through the Severo Ochoa Program for Centers of Excellence for the FUNFUTURE (EX2019-000917-S project), and by the Generalitat de Catalunya (2021/SGR/00286, 2021/SGR/00442). E. R. thanks Generalitat de Catalunya by an ICREA Academia award, Spanish Ministry Science for a Maria de Maeztu excellence grant (CEX2021-001202-M) and computer resources, technical expertise and assistance provided by the CSUC. Zhen Li acknowledges the China Scholarship Council (CSC) for his PhD grant (201808310071) and Scientific Research Foundation of Dezhou University (2023xjrc210). The present publication is dedicated to Prof. John D. Kennedy on the occasion of his 80th Birthday. Yin-yang symbol via Flickr (CC BY 2.0 licence).

References

1 Y.-C. Wei, K.-H. Kuo, Y. Chi and P.-T. Chou, *Acc. Chem. Res.*, 2023, **56**, 689–699.

2 T. Mehmood and J. P. Reddy, in *Advances in aggregation induced emission materials in biosensing and imaging for biomedical applications, PT B*, ed. R. S. Bhosale and V. Singh, 2021, vol. 185, pp. 179–198.

3 C. Chiatti, C. Fabiani and A. L. Pisello, in *Annual review of materials research*, ed. D. R. Clarke, 2021, vol. 51, pp. 409–433.

4 S. Gao, Z. Cui and F. Li, *Chem. Soc. Rev.*, 2023, **52**, 2875–2885.

5 J. Liu, J. Xue, G.-P. Yang, L.-L. Dang, L.-F. Ma, D.-S. Li and Y.-Y. Wang, *Coord. Chem. Rev.*, 2022, **463**, 214521.

6 Z. Zhao, J. W. Y. Lam and B. Z. Tang, *Soft Matter*, 2013, **9**, 4564–4579.

7 R. Núñez, I. Romero, F. Teixidor and C. Viñas, *Chem. Soc. Rev.*, 2016, **45**, 5147–5173.

8 A. M. Spokoyny, C. W. Machan, D. J. Clingerman, M. S. Rosen, M. J. Wiester, R. D. Kennedy, C. L. Stern, A. A. Sarjeant and C. A. Mirkin, *Nat. Chem.*, 2011, **3**, 590–596.

9 R. Núñez, M. Tarrés, A. Ferrer-Ugalde, F. F. de Biani and F. Teixidor, *Chem. Rev.*, 2016, **116**, 14307–14378.

10 M. Scholz and E. Hey-Hawkins, *Chem. Rev.*, 2011, **111**, 7035–7062.

11 F. Issa, M. Kassiou and L. M. Rendina, *Chem. Rev.*, 2011, **111**, 5701–5722.

12 A. M. Spokoyny, *Pure Appl. Chem.*, 2013, **85**, 903–919.

13 S. P. Fisher, A. W. Tomich, S. O. Lovera, J. F. Kleinsasser, J. Guo, M. J. Asay, H. M. Nelson and V. Lavallo, *Chem. Rev.*, 2019, **119**, 8262–8290.

14 J. Poater, C. Viñas, I. Bennour, S. Escayola, M. Solà and F. Teixidor, *J. Am. Chem. Soc.*, 2020, **142**, 9396–9407.

15 J. Poater, M. Solà, C. Viñas and F. Teixidor, *Angew. Chem., Int. Ed.*, 2014, **53**, 12191–12195.

16 J. Poater, C. Viñas, M. Solà and F. Teixidor, *Nat. Commun.*, 2022, **13**, 3844.

17 J. Plesek, *Chem. Rev.*, 1992, **92**, 269–278.

18 R. N. Grimes, *Carboranes*, Academic Press, 2016.

19 F. Teixidor and D. E. Kaufmann, *Science of Synthesis: Houben-Weyl Methods of Molecular Transformations*, Georg Thieme Verlag, Stuttgart, 5th edn, 2015, vol. 6.

20 S. Fujii, *MedChemComm*, 2016, **7**, 1082–1092.

21 J. F. Valliant, K. J. Guenther, A. S. King, P. Morel, P. Schaffer, O. O. Sogbein and K. A. Stephenson, *Coord. Chem. Rev.*, 2002, **232**, 173–230.

22 P. Labra-Vázquez, R. Flores-Cruz, A. Galindo-Hernández, J. Cabrera-González, C. Guzmán-Cedillo, A. Jiménez-Sánchez, P. G. Lacroix, R. Santillan, N. Farfán and R. Núñez, *Chem. – Eur. J.*, 2020, **26**, 16530–16540.

23 X. Wu, J. Guo, Y. Quan, W. Jia, D. Jia, Y. Chen and Z. Xie, *J. Mater. Chem. C*, 2018, **6**, 4140–4149.

24 S.-Y. Kim, J.-D. Lee, Y.-J. Cho, M. R. Son, H.-J. Son, D. W. Cho and S. O. Kang, *Phys. Chem. Chem. Phys.*, 2018, **20**, 17458–17463.

25 K. Nishino, H. Yamamoto, J. Ochi, K. Tanaka and Y. Chujo, *Chem. – Asian J.*, 2019, **14**, 1577–1581.

26 D. K. You, H. So, C. H. Ryu, M. Kim and K. M. Lee, *Chem. Sci.*, 2021, **12**, 8411–8423.

27 C. Bellomo, D. Zanetti, F. Cardano, S. Sinha, M. Chaari, A. Fin, A. Maranzana, R. Núñez, M. Blangetti and C. Prandi, *Dyes Pigm.*, 2021, **194**, 109644.

28 L. Ji, S. Riese, A. Schmiedel, M. Holzapfel, M. Fest, J. Nitsch, B. F. E. Curchod, A. Friedrich, L. Wu, H. H. Al Mamari, S. Hammer, J. Pflaum, M. A. Fox, D. J. Tozer, M. Finze, C. Lambert and T. B. Marder, *Chem. Sci.*, 2022, **13**, 5205–5219.

29 J. Ochi, K. Tanaka and Y. Chujo, *Dalton Trans.*, 2021, **50**, 1025–1033.

30 K. L. Martin, J. N. Smith, E. R. Young and K. R. Carter, *Macromolecules*, 2019, **52**, 7951–7960.

31 D. Tu, S. Cai, C. Fernandez, H. Ma, X. Wang, H. Wang, C. Ma, H. Yan, C. Lu and Z. An, *Angew. Chem., Int. Ed.*, 2019, **58**, 9129–9133.

32 X. Wu, J. Guo, Y. Cao, J. Zhao, W. Jia, Y. Chen and D. Jia, *Chem. Sci.*, 2018, **9**, 5270–5277.

33 J. Ochi, K. Tanaka and Y. Chujo, *Angew. Chem., Int. Ed.*, 2020, **59**, 9841–9855.

34 Z. Wang, J. Zhao, M. Muddassir, R. Guan and S. Tao, *Inorg. Chem.*, 2021, **60**, 4705–4716.

35 K. Yuhara, K. Tanaka and Y. Chujo, *Mater. Chem. Front.*, 2022, **6**, 1414–1420.

36 F. Sun, S. Tan, H.-J. Cao, J. Xu, V. I. Bregadze, D. Tu, C. Lu and H. Yan, *Angew. Chem., Int. Ed.*, 2022, **61**, e202207125.

37 J. Tong, Y. Cao, Y.-W. Zhang, P. Wang, P. Wang, X.-J. Liao, W. Zhang, Y. Wang, Y.-X. Zheng, J.-J. Zhu and Y. Pan, *Angew. Chem., Int. Ed.*, 2022, **61**, e202209438.

38 Z. Wang, B. Chen, H. Zhang, H. Yang, S. Tao and R. Guan, *Mater. Chem. Front.*, 2022, **6**, 783–792.

39 K. Tanaka, M. Gon, S. Ito, J. Ochi and Y. Chujo, *Coord. Chem. Rev.*, 2022, **472**, 214779.

40 S. Sinha, Z. Kelemen, E. Hümpfner, I. Ratera, J.-P. Malval, J. P. Jurado, C. Viñas, F. Teixidor and R. Núñez, *Chem. Commun.*, 2022, **58**, 4016–4019.

41 J. Soldevila-Sanmartín, E. Ruiz, D. Choquesillo-Lazarte, M. E. Light, C. Viñas, F. Teixidor, R. Núñez, J. Pons and J. G. Planas, *J. Mater. Chem. C*, 2021, **9**, 7643–7657.

42 Z. Li, R. Núñez, M. E. Light, E. Ruiz, F. Teixidor, C. Viñas, D. Ruiz-Molina, C. Roscini and J. G. Planas, *Chem. Mater.*, 2022, **34**, 4795–4808.

43 D. Tu, J. Li, F. Sun, H. Yan, J. Poater and M. Solà, *JACS Au*, 2021, **1**, 2047–2057.

44 A. Jana, M. Jash, W. A. Dar, J. Roy, P. Chakraborty, G. Paramasivam, S. Lebedkin, K. Kirakci, S. Manna, S. Antharjanam, J. Machacek, M. Kucerakova, S. Ghosh, K. Lang, M. M. Kappes, T. Base and T. Pradeep, *Chem. Sci.*, 2023, **14**, 1613–1626.

45 J. Cabrera-González, A. Ferrer-Ugalde, S. Bhattacharyya, M. Chaari, F. Teixidor, J. Gierschner and R. Núñez, *J. Mater. Chem. C*, 2017, **5**, 10211–10219.

46 A. Ferrer-Ugalde, J. Cabrera-González, E. J. Juárez-Pérez, F. Teixidor, E. Pérez-Inestrosa, J. M. Montenegro, R. Sillanpää, M. Haukka and R. Núñez, *Dalton Trans.*, 2017, **46**, 2091–2104.

47 M. Chaari, Z. Kelemen, J. G. Planas, F. Teixidor, D. Choquesillo-Lazarte, A. Ben Salah, C. Viñas and R. Núñez, *J. Mater. Chem. C*, 2018, **6**, 11336–11347.

48 M. Chaari, Z. Kelemen, D. Choquesillo-Lazarte, N. Gaztelumendi, F. Teixidor, C. Viñas, C. Nogués and R. Núñez, *Biomater. Sci.*, 2019, **7**, 5324–5337.

49 L. Schwartz, L. Eriksson, R. Lomoth, F. Teixidor, C. Viñas and S. Ott, *Dalton Trans.*, 2008, 2379–2381.

50 F. Teixidor, R. Núñez, C. Viñas, R. Sillanpää and R. Kivekäs, *Angew. Chem., Int. Ed.*, 2000, **39**, 4290–4292.

51 R. Núñez, P. Farràs, F. Teixidor, C. Viñas, R. Sillanpää and R. Kivekäs, *Angew. Chem., Int. Ed.*, 2006, **45**, 1270–1272.

52 P. J. Stephens, F. J. Devlin, C. F. Chabalowski and M. J. Frisch, *J. Phys. Chem.*, 1994, **98**, 11623–11627.

53 J. Bae, M. Sakai, Y. Tsuchiya, N. Ando, X. K. Chen, T. B. Nguyen, C. Y. Chan, Y. T. Lee, M. Auffray, H. Nakanotani, S. Yamaguchi and C. Adachi, *Front. Chem.*, 2022, **10**, DOI: 10.3389/fchem.2022.990918.

54 C. Fang, B. Oruganti and B. Durbeej, *J. Phys. Chem. A*, 2014, **118**, 4157–4171.

55 P. Rybczyński, M. H. E. Bousquet, A. Kaczmarek-Kędziera, B. Jędrzejewska, D. Jacquemin and B. Ośmiałowski, *Chem. Sci.*, 2022, **13**, 13347–13360.

56 K. Ikemoto, T. Tokuhira, A. Uetani, Y. Harabuchi, S. Sato, S. Maeda and H. Isobe, *J. Org. Chem.*, 2020, **85**, 150–157.

57 Y. Harabuchi, M. Hatanaka and S. Maeda, *Chem. Phys. Lett.*, 2019, **737**, 100007.

58 Y. Harabuchi, T. Taketsugu and S. Maeda, *Phys. Chem. Chem. Phys.*, 2015, **17**, 22561–22565.

59 Y. Cui, Y. Yue, G. Qian and B. Chen, *Chem. Rev.*, 2012, **112**, 1126–1162.

60 T. Gorai, W. Schmitt and T. Gunnlaugsson, *Dalton Trans.*, 2021, **50**, 770–784.

61 P. A. Tanner, W. Thor, Y. Zhang and K.-L. Wong, *J. Phys. Chem. A*, 2022, **126**, 7418–7431.

62 E. Kasprzycka, V. A. Trush, V. M. Amirkhanov, L. Jerzykiewicz, O. L. Malta, J. Legendziewicz and P. Gawryszewska, *Chem. – Eur. J.*, 2017, **23**, 1318–1330.

63 C. Yang, L.-M. Fu, Y. Wang, J.-P. Zhang, W.-T. Wong, X.-C. Ai, Y.-F. Qiao, B.-S. Zou and L.-L. Gui, *Angew. Chem., Int. Ed.*, 2004, **43**, 5010–5013.

64 Z. Li, X.-B. Li, M. E. Light, A. E. Carrillo, A. Arauzo, M. Valvidares, C. Roscini, F. Teixidor, C. Viñas, F. Gándara, E. Bartolomé and J. G. Planas, *Adv. Funct. Mater.*, 2023, **33**, 2307369.

65 L. Armelao, S. Quici, F. Barigelletti, G. Accorsi, G. Bottaro, M. Cavazzini and E. Tondello, *Coord. Chem. Rev.*, 2010, **254**, 487–505.

66 E. J. Peterson, J. Rawson, D. N. Beratan, P. Zhang and M. J. Therien, *J. Am. Chem. Soc.*, 2022, **144**, 15457–15461.

67 H. Uoyama, K. Goushi, K. Shizu, H. Nomura and C. Adachi, *Nature*, 2012, **492**, 234–238.

68 T. Chen, L. Zheng, J. Yuan, Z. An, R. Chen, Y. Tao, H. Li, X. Xie and W. Huang, *Sci. Rep.*, 2015, **5**, 10923.

69 J. Zhao, W. Wu, J. Sun and S. Guo, *Chem. Soc. Rev.*, 2013, **42**, 5323–5351.

70 S. Xu, Y. Yuan, X. Cai, C.-J. Zhang, F. Hu, J. Liang, G. Zhang, D. Zhang and B. Liu, *Chem. Sci.*, 2015, **6**, 5824–5830.

71 F. Neese, *WIREs Comput. Mol. Sci.*, 2018, **8**, e1327.

72 M. Nooijen and R. J. Bartlett, *J. Chem. Phys.*, 1997, **106**, 6441–6448.

73 M. Nooijen and R. J. Bartlett, *J. Chem. Phys.*, 1997, **107**, 6812–6830.

74 F. Weigend and R. Ahlrichs, *Phys. Chem. Chem. Phys.*, 2005, **7**, 3297–3305.

75 J. Sous, P. Goel and M. Nooijen, *Mol. Phys.*, 2014, **112**, 616–638.

76 A. K. Dutta, F. Neese and R. Izsák, *J. Chem. Phys.*, 2016, **145**, 34102.

77 A. K. Dutta, M. Nooijen, F. Neese and R. Izsák, *J. Chem. Phys.*, 2017, **146**, 74103.

78 A. K. Dutta, M. Nooijen, F. Neese and R. Izsák, *J. Chem. Theory Comput.*, 2018, **14**, 72–91.

79 F. Weigend, *Phys. Chem. Chem. Phys.*, 2006, **8**, 1057–1065.

80 M. J. Frisch, G. W. Trucks, H. B. Schlegel, G. E. Scuseria, M. A. Robb, J. R. Cheeseman, G. Scalmani, V. Barone, G. A. Petersson, H. Nakatsuji, X. Li, M. Caricato, A. V. Marenich, J. Bloino, B. G. Janesko, R. Gomperts, B. Mennucci, H. P. Hratchian, J. V. Ortiz, A. F. Izmaylov, J. L. Sonnenberg, D. Williams-Young, F. Ding, F. Lipparini, F. Egidi, J. Goings, B. Peng, A. Petrone, T. Henderson, D. Ranasinghe, V. G. Zakrzewski, J. Gao, N. Rega, G. Zheng, W. Liang, M. Hada, M. Ehara, K. Toyota, R. Fukuda, J. Hasegawa, M. Ishida, T. Nakajima, Y. Honda, O. Kitao, H. Nakai, T. Vreven, K. Throssell, J. A. Montgomery Jr., J. E. Peralta, F. Ogliaro, M. J. Bearpark, J. J. Heyd, E. N. Brothers, K. N. Kudin, V. N. Staroverov, T. A. Keith, R. Kobayashi, J. Normand, K. Raghavachari, A. P. Rendell, J. C. Burant, S. S. Iyengar, J. Tomasi, M. Cossi, J. M. Millam, M. Klene, C. Adamo, R. Cammi, J. W. Ochterski, R. L. Martin, K. Morokuma, O. Farkas, J. B. Foresman and D. J. Fox, *Gaussian 16, Revision C.01*, Gaussian, Inc., Wallingford, 2016.

81 A. D. Becke, *J. Chem. Phys.*, 1993, **98**, 5648–5652.